Queensland University of Technology
Brisbane Australia

This may be the author's version of a work that was submitted/accepted for publication in the following source:

Roy, Sourav, Kiratnia, Sharadindu Gopal, Roy, Priyo Nath, Hasan, Md. Mahmudul, Howlader, Ashraful Hossain, Rahman, Md. Shohanur, Islam, Md. Rafiqul, Rana, Md. Masud, Abdulrazak, Lway Faisal, Mehedi, Ibrahim Mustafa, Islam, Md. Shofiqul, & Hossain, Md. Biplob
(2020)
Numerical Investigation into Optoelectronic Performance of InGaN Blue Laser in Polar, Non-Polar and Semipolar Crystal Orientation.
Crystals, *10*(11), Article number: 1033 1-24.

This file was downloaded from: https://eprints.qut.edu.au/211136/

© 2020 The Author(s)

This work is covered by copyright. Unless the document is being made available under a Creative Commons Licence, you must assume that re-use is limited to personal use and that permission from the copyright owner must be obtained for all other uses. If the document is available under a Creative Commons License (or other specified license) then refer to the Licence for details of permitted re-use. It is a condition of access that users recognise and abide by the legal requirements associated with these rights. If you believe that this work infringes copyright please provide details by email to qut.copyright@qut.edu.au

License: Creative Commons: Attribution 4.0

Notice: *Please note that this document may not be the Version of Record (i.e. published version) of the work. Author manuscript versions (as Submitted for peer review or as Accepted for publication after peer review) can be identified by an absence of publisher branding and/or typeset appearance. If there is any doubt, please refer to the published source.*

https://doi.org/10.3390/cryst10111033

Article

Numerical Investigation into Optoelectronic Performance of InGaN Blue Laser in Polar, Non-Polar and Semipolar Crystal Orientation

Sourav Roy [1,*], Sharadindu Gopal Kiratnia [2], Priyo Nath Roy [1], Md. Mahmudul Hasan [3], Ashraful Hossain Howlader [4], Md. Shohanur Rahman [1], Md. Rafiqul Islam [5], Md. Masud Rana [2], Lway Faisal Abdulrazak [6,7], Ibrahim Mustafa Mehedi [8,9], Md. Shofiqul Islam [8] and Md. Biplob Hossain [2]

[1] Department of Mechatronics Engineering, Khulna University of Engineering & Technology, Khulna 9203, Bangladesh; priyo@mte.kuet.ac.bd (P.N.R.); shohan@mte.kuet.ac.bd (M.S.R.)
[2] Department of Electrical & Electronic Engineering, Jashore University of Science & Technology, Jashore 7408, Bangladesh; s.kirtania@just.edu.bd (S.G.K.); mm.rana@just.edu.bd (M.M.R.); biplobh.eee10@gmail.com (M.B.H.)
[3] Centre for Accident Research & Road Safety-Queensland (CARRS-Q), Queensland University of Technology, Brisbane, Queensland 4059, Australia; m8.hasan@hdr.qut.edu.au
[4] School of Physics, The University of Sydney, Sydney, NSW 2006, Australia; ashraful.howlader@sydney.edu.au
[5] Department of Electrical & Electronic Engineering, Khulna University of Engineering & Technology, Khulna 9203, Bangladesh; mri@eee.kuet.ac.bd
[6] Department of Computer Science, Cihan University Sulaimaniya, Sulaimaniya 46001, Iraq; lway.faisal@sulcihan.edu.krd
[7] Electrical Engineering Department, College of Engineering, University of Sulaimani, Sulaimaniya 46001, Iraq
[8] Department of Electrical & Computer Engineering, King Abdulaziz University, Jeddah 21589, Saudi Arabia; imehedi@kau.edu.sa (I.M.M.); msislam@kau.edu.sa (M.S.I.)
[9] Center of Excellence in Intelligent Engineering Systems (CEIES), King Abdulaziz University, Jeddah 21589, Saudi Arabia
* Correspondence: souravroy2k9@gmail.com

Received: 22 September 2020; Accepted: 10 November 2020; Published: 13 November 2020

Abstract: Recently, InGaN grown on semipolar and non-polar orientation has caused special attraction due to reduction in the built-in polarization field and increased confinement of high energy states compared to traditional polar c-plane orientation. However, any widespread-accepted report on output power and frequency response of the InGaN blue laser in non-c-plane orientation is readily unavailable. This work strives to address an exhaustive numerical investigation into the optoelectronic performance and frequency response of $In_{0.17}Ga_{0.83}N$/GaN quantum well laser in polar (0001), non-polar $(10\bar{1}0)$ and semipolar $(10\bar{1}2)$, $(11\bar{2}2)$ and $(10\bar{1}1)$ orientations by working out a 6×6 k.p Hamiltonian at the Γ-point using the tensor rotation technique. It is noticed that there is a considerable dependency of the piezoelectric field, energy band gap, peak optical gain, differential gain and output power on the modification in crystal orientation. Topmost optical gain of 4367 cm^{-1} is evaluated in the semipolar $(11\bar{2}2)$-oriented laser system at an emission wavelength of 448 nm when the injection carrier density is 3.7×10^{18} cm^{-3}. Highest lasing power and lowest threshold current are reported to be 4.08 mW and 1.45 mA in semipolar $(11\bar{2}2)$ crystal orientation. A state-space model is formed in order to achieve the frequency response which indicates the highest magnitude (dB) response in semipolar $(11\bar{2}2)$ crystal orientation.

Keywords: blue laser; frequency response; InGaN; quantum confined stark effect; semipolar orientation; valence band

1. Introduction

A III-N Wurtzite (WZ) ternary semiconductor alloy like InGaN has emerged as a remarkably attractive material for optoelectronic devices over the last era due to broad bandgap span (0.7 eV–3.4 eV), magnificent electron mobility, thermal conductivity, chemical and thermal stability, breakdown field and saturation drift velocity [1]. By tuning indium (In) composition of $In_xGa_{1-x}N$ quantum well (QW) in the active region, InGaN/GaN-based laser and light emitting diodes (LEDs) can efficiently emit light between green and violet spectrum range [2]. For true-blue light emission, laser oscillating at a wavelength of 440~450 nm is required. Blue laser imaging constructs superb images useful for the detection and thorough examination of upper gastrointestinal lesions [3]. Since a blue laser is capable of storing and reading two to four times the amount of data than a red laser, its typical application range extends up to the functioning of high-density optical storage systems, high-resolution laser printers, barcode scanners, Light Detection and Ranging (LIDARs) and temperature sensors, etc. [4].

Following the development of the first blue LED by Nakamura et al. in 1990s [5], most of the research works to date have highlighted polar c-plane (0001)-oriented III-N heterostructures mainly for availability of high-quality substrates. However, the growth of the InGaN blue laser in polar orientation faces several challenges, ostensibly from the presence of the internal polarization field. Built-in spontaneous polarization (SP) plus biaxial compressive strain-assisted piezoelectric polarization (PZ) introduces an electric field at InGaN/GaN heterojunction that bends the energy bands. The hole and electron wave functions shift in opposite directions due to such band bending, and the emanating spatial separation of confined carriers decrease oscillator strength and transition probability of the bound states [6]. The phenomenon is termed as quantum-confined stark effect (QCSE), as shown in Figure 1. Furthermore, high injection carrier density is required for polar-oriented QW in order to produce significant optical gain due to closely-spaced heavy-hole and light-hole bands at the gamma (Γ)-point [7]. Thus, control of the internal fields in strained layers is essential with a view to realize high power and high-speed InGaN-based optoelectronics.

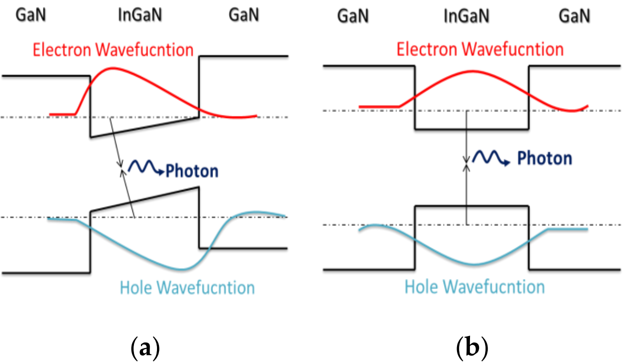

Figure 1. Visualization of quantum-confined stark effect (QCSE) in InGaN/GaN quantum well (QW). Structure (**a**) suffers from QCSE while (**b**) is free from it.

Recently, it has become evident that in lieu of conventional polar c-plane (0001)-orientation, non-polar- and semipolar-oriented III-N structures diminish or eliminate the internal polarization field and related QCSE [8,9]. Hence, several basic and applied disquisitions on non-c-plane-oriented growth of GaN and InGaN have been reported over the last few years thanks to plasma-assisted Molecular Beam Epitaxy (MBE) and Metal-Organic Chemical Vapor Deposition (MOCVD). Semipolar $(11\bar{2}2)$ and $(20\bar{2}\bar{1})$-oriented blue laser diodes grown on sapphire substrate and lasing at peak wavelength of 439 and 456 nm were reported for the first time [10,11]. The optical properties of non-polar m-plane $In_xGa_{1-x}N$ ($x \leq 0.21$) thin films have been characterized by Cao et al. via photoluminescence spectroscopy [12]. A work by Xing et al. demonstrated semipolar $(11\bar{2}2)$-oriented GaN epitaxial film growth on m-plane sapphire substrate with significantly reduced defect densities [13]. Senichev et al. studied the impact of growth conditions and strain state on the structural and optical properties of non-polar m-plane

$(10\bar{1}0)$-oriented InGaN with In composition up to 39% [14]. Sawicka et al. reported the growth of semipolar $(20\bar{2}1)$ and non-polar $(10\bar{1}0)$-oriented InGaN growth with low In composition [15]. Song et al. documented the growth of semipolar $(20\bar{2}1)$-oriented InGaN LED on sapphire substrate [16]. To date, the optical gain profile and subsequent power-current and frequency response of InGaN QW-based true blue laser in non-polar and semipolar orientations have not been studied in detail.

In this paper, the key optoelectronic properties such as energy band diagram, optical gain profile, output power and frequency response of compressively strained $In_{0.17}Ga_{0.83}N$/GaN QW true blue laser (λ = 445 nm) have been studied in the presence of the PZ-polarized field along polar (0001), non-polar $(10\bar{1}0)$ and semipolar $(10\bar{1}2)$, $(11\bar{2}2)$ and $(10\bar{1}1)$ crystal orientations using 6×6 k.p Hamiltonian at Γ-point. For accurate calculation of bandgap energy, temperature-dependent bandgap shrinkage phenomenon is introduced. To explore the significant features in non-polar and semipolar orientations, tensor rotation formula is mastered to alter the 6×6 k.p Hamiltonian matrix from (0001) crystal orientation. The finite difference technique is utilized in order to evaluate valence and conduction band Eigen energies and wave functions. The optical gain profile is determined from the momentum matrix elements of charge carriers and interband coupling of valence subbands. The output lasing power characteristics are evaluated by a Simulink model based on two-level laser rate equations. An electron drift-leakage model is integrated into a recombination rate equation to depict efficiency droop phenomenon comprehensively. Frequency response is estimated from the bode plot based on state-space representation of QW laser. The results presented here are obtained at 300K. Figure 2 shows the schematic representation of some of the polar, non-polar and semipolar orientations for WZ InGaN.

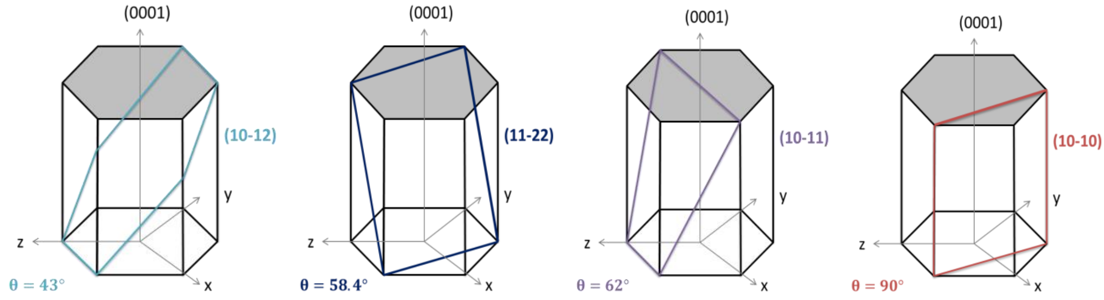

Figure 2. Schematic representation of semipolar $(10\bar{1}2)$, $(11\bar{2}2)$, $(10\bar{1}1)$ and non-polar $(10\bar{1}0)$ orientations for WZ InGaN. The shaded area marks polar (0001) orientation. Crystal angle θ is defined as the angle between growth-axis and the c-axis.

The paper is organized as follows: computational details to determine the key optoelectronic properties for the InGaN QW laser are demonstrated in segment 3. Results and discussion relevant to orientation-dependent band gap energy, output power and frequency response are illustrated in segment 4. This segment also contains the verifications of the simulation model with published results on the InGaN QW-based green laser (λ > 500 nm) in polar and semipolar orientations. Convincingly, a summary is encapsulated in segment 5.

2. Materials and Methods

2.1. Laser Structure

The numerical simulation of a reference single QW (SQW) laser structure (Figure 3) is considered to study the non-c-axis-oriented InGaN blue laser optoelectronic performance [17]. This laser structure has been developed by Sharp Corporation at Devices Technology Research Laboratories located in Nara, Japan. It is grown on GaN substrate. The active and barrier layers of the device are formed by 8 nm thick undoped $In_{0.17}Ga_{0.83}N$ and 10 nm thick Si-doped GaN, respectively. The structure is also composed of n and p-type InGaN buffer layer in order to maintain low spontaneous emission, n and p-type $Al_{0.1}Ga_{0.9}N$ top/bottom cladding layer to confine carrier spillover, n and p-type GaN

top/bottom optical guiding layer and a p-type $Al_{0.3}Ga_{0.7}N$ evaporation-prevention layer. An oxide aperture is deposited above the upper AlGaN layer for current and index confinement [17]. In the proposed laser system, the active region material has (hkil) orientation, and all other layers are in (0001) orientation. In order to avoid structural degradation, the direct wafer bonding technique is assumed to join the interface of (0001) and (hkil)-oriented layers [18–20].

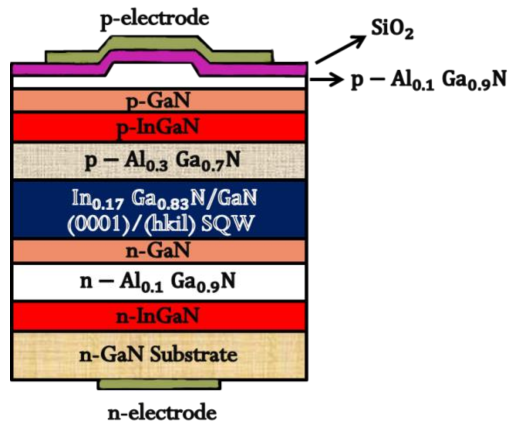

Figure 3. Structure of $In_{0.17}Ga_{0.83}N/GaN$ single QW (SQW) blue laser.

The composition-dependent energy gap, E_g for $In_xGa_{1-x}N$ can be given by [21]:

$$E_g(In_xGa_{1-x}N) = (1-x)E_g^{GaN}(T) + xE_g^{InN}(T) - 1.43x(1-x) \quad (1)$$

Here, $E_g^{GaN}(T)$ and $E_g^{InN}(T)$ describe the non-linear dependencies of the energy band gap on temperature (band gap narrowing (BGN)) for GaN and InN epilayers. The temperature-dependent band gap of GaN is given by semiempirical relations of "(2)" which is based on electron–phonon interaction and average phonon occupation number [22].

$$E_g^{GaN}(T) = E_g^{GaN}(T = 0\,K) - \zeta\Theta_p\left[\frac{1-\chi}{e^{\left(\frac{\Theta_p}{T}\right)}-1} + \frac{\chi}{4}\left(\sqrt[4]{1+\frac{\pi^2}{6}\left(\frac{4T}{\Theta_p}\right)^2+\left(\frac{4T}{\Theta_p}\right)^4}-1\right)\right] \quad (2)$$

Here, $E_g^{GaN}(T = 0\,K) = 3.47$ eV, bandgap temperature coefficient $\zeta = 0.612$ meV/K, phonon temperature $\Theta_p = 728$ K, degree of phonon dispersion $\chi = 0.42$.

The temperature-dependent band gap of InN is calculated with *Varshini*'s law of "(3)" since the overall impact of electron–phonon interaction on InN energy gap is considerably weaker than GaN [23].

$$E_g^{InN}(T) = E_g^{InN}(T = 0\,K) - \frac{\alpha_{var}T^2}{\beta_{var}+T} \quad (3)$$

Here, $E_g^{InN}(T = 0\,K) = 0.69$ eV, $\alpha_{var} = 0.41$ meV/K and $\beta_{var} = 454$ K

The bandgap of GaN and InN at room temperature with BGN is found to be 3.403 and 0.64 eV, respectively.

2.2. Crystal Orientation-Dependent Energy Band Dispersion Profile

Parabolic conduction band (CB) dispersion profile is presumed throughout this work. 1-D Schrödinger equation for conduction band in order to find discrete energy levels of QW is given below [24]:

$$\left[\frac{-\hbar^2}{2m_e^*}\frac{d^2}{dz^2} + v_e(z)\right]\psi_n(z) = E_e(k_t = 0)\psi_n(z) \quad (4)$$

Here, conduction band wave function is $\psi_n(z)$, $\hbar$ is reduced Planck's constant, effective mass of the electron is m_e^*, E_e gives electron energy level and k_t is inplane wave vector. $v_e(z)$ is conduction band potential which is expressed by:

$$v_e = \begin{vmatrix} a_{cz}\varepsilon_{zz} + a_{ct}\left(\varepsilon_{xx} + \varepsilon_{yy}\right) & |z| \le \frac{L_w}{2} \\ \Delta v_e & |z| \ge \frac{L_w}{2} \end{vmatrix} \quad (5)$$

Here, L_w is the QW length, a_{cz} and a_{ct} are the deformation potentials for CB along the c axis and perpendicular to the c axis, ε_{ij} are the principal strain components, Δv_e is the barrier layer conduction band offset. We take $a_{cz} = a_{ct}$ for simplicity. Eigen function and Eigen energy for the conduction band at Γ-point are evaluated by finite difference discretization. The conduction band energy dispersion relation is found from the following equation:

$$E(k) = \frac{\hbar^2}{2}\left(\frac{{k_x}^2 + {k_y}^2}{{m_e}^t} + \frac{{k_z}^2}{{m_e}^z}\right) + {E_c}^0 \quad (6)$$

Here, k_x, k_y and k_z are the wave vectors and ${E_c}^0$ accounts for bandedge energy.

The valence band structure for (0001) orientation is solved by using a 6×6 k.p Hamiltonian matrix H with means of finite difference scheme. The Rashba–Sheka–Pikus (RSP) six-band matrix for (0001) WZ crystal is given by [25]:

$$H\psi_h(z) = E\psi_h \quad (7)$$

The components of H and $\psi_h(z)$ are:

$$H(k,\varepsilon) = \begin{bmatrix} F & -K^* & -H^* & 0 & 0 & 0 \\ -K & G & H & 0 & 0 & \Delta \\ -H & -H^* & \lambda & 0 & \Delta & 0 \\ 0 & 0 & 0 & F & -K & H \\ 0 & 0 & \Delta & -K^* & G & H \\ 0 & \Delta & 0 & H^* & -H & \lambda \end{bmatrix} \quad (8)$$

$$\Psi_h(z) = \begin{bmatrix} \phi_{\frac{3}{2},\frac{3}{2}}(z) \\ \phi_{\frac{3}{2},\frac{1}{2}}(z) \\ \phi_{\frac{1}{2},\frac{1}{2}}(z) \\ \phi_{\frac{3}{2},\frac{-3}{2}}(z) \\ \phi_{\frac{3}{2},\frac{-1}{2}}(z) \\ \phi_{\frac{1}{2},\frac{-1}{2}}(z) \end{bmatrix} = \begin{bmatrix} g^{(1)}(z) \\ g^{(2)}(z) \\ g^{(3)}(z) \\ g^{(4)}(z) \\ g^{(5)}(z) \\ g^{(6)}(z) \end{bmatrix}$$

ϕ_{j,m_j} or $g^{(j)}$ is the wave function components for valence band and E is the energy of heavy hole (HH), light hole (LH) and crystal field split-off holes (CH). The matrix elements are:

$$F = \Delta_1 + \Delta_2 + \lambda + \theta$$

$$G = \Delta_1 - \Delta_2 + \lambda + \theta$$

$$\Delta = \sqrt{2}\Delta_3$$

$$\lambda = \frac{\hbar^2}{2m_0}\left[A_1 k_z^2 + A_2\left(k_x^2 + k_y^2\right)\right] + D_1\varepsilon_{zz} + D_2(\varepsilon_{xx} + \varepsilon_{yy})$$

$$\theta = \frac{\hbar^2}{2m_0}\left[A_3 k_z^2 + A_4\left(k_x^2 + k_y^2\right)\right] + D_3\varepsilon_{zz} + D_4(\varepsilon_{xx} + \varepsilon_{yy})$$

$$K = \frac{\hbar^2}{2m_0}A_5\left(k_x + ik_y\right)^2 + D_5(\varepsilon_{xx} - \varepsilon_{yy})$$

$$H = \frac{\hbar^2}{2m_0}A_6\left(k_x + ik_y\right)k_z + D_6(\varepsilon_{zx} + i\varepsilon_{yz})$$

Here, D_i's give the deformation potentials for WZ crystals; A_i's indicate the effective-mass parameters of valence band; ε_{ij} are the strain tensors; Δ_1, Δ_2 and Δ_3 account for the crystal-field-split energy and spin-orbit interactions.

The following formula of the rotation matrix is used to find wave vector in non-c-plane (hkil) crystal orientation [26]:

$$O_R = \begin{pmatrix} cos\theta cos\phi & -sin\phi & sin\theta cos\phi \\ cos\theta sin\phi & cos\phi & sin\theta sin\phi \\ -sin\theta & 0 & cos\theta \end{pmatrix} \tag{9}$$

where $\theta = \cos^{-1}(\frac{\sqrt{3}al}{\sqrt{4c^2(h^2+k^2+hk)+3a^2l^2}})$; $\phi = \tan^{-1}\frac{ik}{h}$.

Here, in-plane and out of plane lattice constants for hexagonal structure are noted by a and c, respectively.

We assume the inclination angle θ reliance of physical parameters only due to the hexagonal symmetry. Transformation of the basis states into (x′,y′,z′) coordinates from (x,y,z) coordinates is accomplished by rotation of the angle θ. The z axis points along the c-direction, and z′ is perpendicular to the growth plane (hkil) as shown in Figure 4.

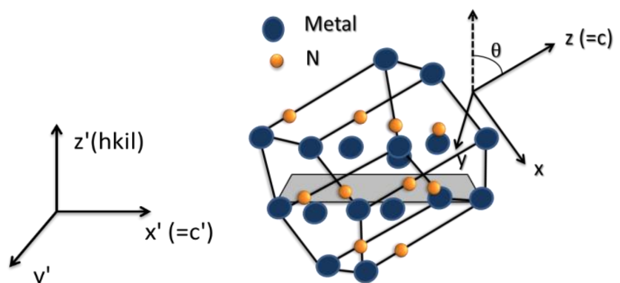

Figure 4. Configuration of the two coordinate systems (x,y,z) and (x′,y′,z′) used to describe non-c-plane QW growth. The shaded area denotes (hkil) orientation.

The strain tensor ε is related with inclination angle θ as follows [27]:

$$\varepsilon_{xx} = \varepsilon_{xx}{}^{(0)} + \varepsilon_{xz}tan\theta \tag{10}$$

$$\varepsilon_{yy} = \varepsilon_{xx}{}^{(0)} \tag{11}$$

$$\varepsilon_{zz} = \varepsilon_{zz}{}^{(0)} + \varepsilon_{xz}cot\theta \tag{12}$$

$$\varepsilon_{xz} = -\left(\left(c_{11} + c_{12} + c_{13}\frac{\varepsilon_{zz}^{(0)}}{\varepsilon_{xx}^{(0)}}\right)sin^2\theta + \left(2c_{13} + c_{33}\frac{\varepsilon_{zz}^{(0)}}{\varepsilon_{xx}^{(0)}}\right)cos^2\theta\right)\varepsilon_{xx}^{(0)}cos\theta sin\theta \times \frac{1}{c_{11}sin^4\theta + 2(c_{13}+2c_{44})sin^2\theta cos^2\theta + c_{33}cos^4\theta} \tag{13}$$

Here, $\varepsilon_{xx}{}^{(0)} = \frac{a_{well}-a_{barrier}}{a_{barrier}}$ and $\varepsilon_{zz}{}^{(0)} = \frac{c_{well}-c_{barrier}}{c_{barrier}}$.
The other strain constants are zero. c_{ij} are the elastic stiffness constants.
The k.p Hamiltonian in (hkil) orientation is assigned by:

$$H^{(hkil)} = UH^{(0001)}U^* \tag{14}$$

The transformation matrix U is defined as [28]:

$$U = \begin{bmatrix} \alpha^* & 0 & 0 & \alpha & 0 & 0 \\ 0 & \beta & 0 & 0 & \beta^* & 0 \\ 0 & 0 & \beta^* & 0 & 0 & \beta \\ \alpha^* & 0 & 0 & -\alpha & 0 & 0 \\ 0 & \beta & 0 & 0 & -\beta^* & 0 \\ 0 & 0 & -\beta^* & 0 & 0 & \beta \end{bmatrix} \quad (15)$$

Here, $\alpha = \frac{1}{\sqrt{2}} e^{i(3\pi/4)}$ and $\beta = \frac{1}{\sqrt{2}} e^{i(\pi/4)}$.

Hence, we get a six-band k.p matrix along the growth coordinate system (x′,y′,z′) by replacing the Hamiltonian of "(5)" for the (0001) orientation with the transformation relation of "(12)".

2.3. Piezoelectric Field

The PZ polarization P' along (x′,y′,z′) coordinates relies upon the inclination angle θ as follows [29]:

$$P'_z = P_x sin\theta + P_z cos\theta + \left(P_{SP}{}^{QW} - P_{SP}{}^{b}\right) cos\theta \quad (16)$$

$$P'_x = P_x cos\theta - P_z sin\theta;\ P'_y = 0 \quad (17)$$

P_{SP} is the spontaneous polarization and P_x, P_y and P_z are the polarization elements along (x,y,z) coordinates.

$$P_x = 2d_{15}c_{44}\varepsilon_{xz}P_y = 0P_z = [d_{31}(c_{11} + c_{12}) + d_{33}c_{13}]\left(\varepsilon_{xx} + \varepsilon_{yy}\right) + [2d_{31}c_{13} + d_{33}c_{33}]\varepsilon_{zz}$$

The electric field reduces to growth direction z only in case of no external charges. The internal electric field within the barrier and QW is determined from the Gauss law as stated [30]:

$$\varepsilon^{QW} E_z^{QW} - \varepsilon^b E_z^b = -\frac{P'_z}{\varepsilon_0} \quad (18)$$

Here, $\varepsilon^{(QW)}$ and $\varepsilon^{(b)}$ are the permittivity for quantum well and barrier layer, respectively, and ε_0 is the permittivity of vacuum.

From the QCSE theory, the change in energy band profile for quantum well structure due to PZ field can be given by [31]:

$E_c = E_c(E_z = 0) + \Delta E^c$ and $E_h = E_h(E_z = 0) + \Delta E^h$

E_c and E_h are electron and hole energy and ΔE is energy shift due to PZ field which is expressed by:

$$\Delta E = C\frac{m^* e^2 E_z^2 L^4}{\hbar^2};\ C = \frac{1}{8}\left(\frac{1}{3} - \frac{2}{\pi^2}\right)^2 \mathrm{L} = \text{QW length}$$

2.4. Momentum Matrix and Optical Gain Profile

Optical gain profile for QW as a function of energy is demonstrated by [32]:

$$g(E) = \frac{2q^2\hbar}{nE_0 c m_0{}^2 LE} \times \sum_{n,m} \int_0^\infty \frac{\frac{k_t M_{nm}(k_t)\Gamma}{2\pi}}{\left(E_{cn}(k_t) - E_{kpm}(k_t) - E\right)^2 + (\Gamma/2\pi)^2} \left(f_c{}^n - f_v{}^m\right) dk_t \quad (19)$$

Here, $\Gamma = \hbar/\tau$, τ is relaxation time of photon, f_v and f_c express the Fermi levels of valence and conduction bands, M_{nm} is the strained QW momentum matrix element.

$$f_c{}^n(k_t) = \frac{1}{1 + exp\left\{[E_{cn}(k_t) + (m_0/m_e^*)\left(E - (E_{cn}(k_t) - E_{kpm}(k_t))\right) - F_c]/kT\right\}}$$

$$f_v{}^m(k_t) = \frac{1}{1 + exp\left\{[E_{kpm}(k_t) - (m_0/m_h^*)\left(E - (E_{cn}(k_t) - E_{kpm}(k_t)\right)) - F_v]/kT\right\}}$$

In carrier density-dependent quasi-fermi level calculation, it is considered that the injected carrier is electron. The expressions of quasi-fermi levels of conduction and valence bands, F_c and F_v can be given by [22]:

$$F_c = E_{c1}(k_t = 0) + kTln\left(\frac{N_{inj} + n_i}{N_c}\right)$$

$$F_v = E_{kp1}(k_t = 0) - kTln\left(\frac{N_{dop} + n_i}{N_v}\right)$$

where, E_{c1} and E_{kp1} are the first conduction and valence band energy at band edge, N_{inj} is the injected carrier density, N_{dop} is the p-type doping density in the well, n_i is the intrinsic carrier density, N_c and N_v are the density of state of electron and hole for the QW material.

The interband optical momentum-matrix elements in WZ QW structure for transverse electric (TE) and transverse magnetic (TM) polarization of the optical electromagnetic field can be illustrated as follows [22]:

$$M_{nm}(k_t)[TE] = -\frac{1}{\sqrt{2}}g^{(1)}\alpha^* cos\theta\left(\frac{m_0P_2}{\hbar}\right) + \frac{1}{\sqrt{2}}g^{(2)}\beta cos\theta\left(\frac{m_0P_2}{\hbar}\right) - g^{(3)}\beta^* sin\theta\left(\frac{m_0P_1}{\hbar}\right) \quad (20)$$

$$M_{nm}(k_t)[TM] = -\frac{1}{\sqrt{2}}g^{(1)}\alpha^* sin\theta\left(\frac{m_0P_2}{\hbar}\right) + \frac{1}{\sqrt{2}}g^{(2)}\beta sin\theta\left(\frac{m_0P_2}{\hbar}\right) + g^{(3)}\beta^* cos\theta\left(\frac{m_0P_1}{\hbar}\right) \quad (21)$$

The first term is for conduction band (CB)-heavy hole (HH) transition, second term for CB-light hole (LH) transition and third term for CB-crystal field split-off hole (CH) transition. Here,

$$P_1^2 = \frac{\hbar^2}{2m_0}\left(\frac{m_0}{m_e^*} - 1\right)\frac{(E_g + \Delta_1 + \Delta_2)\left(E_g + 2\Delta_2\right) - 2\Delta_3^2}{E_g + 2\Delta_2}$$

$$P_2^2 = \frac{\hbar^2}{2m_0}\left(\frac{m_0}{m_e^*} - 1\right)\frac{E_g[(E_g + \Delta_1 + \Delta_2)\left(E_g + 2\Delta_2\right) - 2\Delta_3^2]}{(E_g + \Delta_1 + \Delta_2)(E_g + \Delta_2) - \Delta_3^2}$$

Key parameters for InN and GaN [33] are listed in Table 1. The properties for $In_xGa_{1\text{-}x}N$ were computed by applying Vagard's law.

Table 1. Key Parameters for GaN and InN.

Symbol	Quantity (Unit)	GaN	InN
a	Lattice Constant (A^0)	3.189	3.544
c		5.185	5.718
n	Refractive Index	2.29	3.2
A_1	Valence band effective mass parameters	−7.24	−15.803
A_2		−0.51	−0.497
A_3		6.73	15.251
A_4		−3.36	−7.151
A_5		−3.35	−7.060
A_6		−4.72	−10.078
Δ_1	Energy parameters (meV)	21	17
Δ_{so}		11	3
$\Delta_2 = \Delta_3 = \Delta_{so}/3$		3.67	1
C_{11}	Elastic Stiffness Constant (GPa)	375	225
C_{12}		140	110
C_{13}		115	95

Table 1. *Cont.*

Symbol	Quantity (Unit)	GaN	InN
C_{33}		385	200
C_{44}		120	45
D_1		−4.08	−3.62
D_2		0.7	−4.60
D_3	Deformation Potentials(eV)	2.1	2.68
D_4		1.4	1.74
D_5		−0.7	−2.07
D_6		−0.7	−2.07
d_{33}		0.65	0.43
d_{31}	Piezoelectric Constant(C/m^2)	−0.33	−0.22
d_{15}		−0.33	−0.22
P_{sp}	Spontaneous Polarization (C/m^2)	−0.029	−0.032
A	Unimolecular recombination rate coefficient (s^{-1})	1×10^7	4×10^7
B	Radiative recombination rate coefficient (cm^{-3} s^{-1})	1.1×10^{-8}	2.0×10^{-10}
C	Auger recombination rate coefficient (cm^{-6} s^{-1})	1.4×10^{-31}	1.05×10^{-31}

2.5. Output Power and Frequency Response

Two-level rate equations which represent carrier confinement in the single QW and Separate Confinement-Heterostructure (SCH)/barrier layers is modeled in Simulink in order to obtain crystal orientation-dependent output power vs. current (P-I) response of InGaN blue laser. This laser model only simulates spontaneous emission of photons region and linear stimulated emission region [34]. The simulation approach is shown in Appendix A.

The rate equations [35] are

$$\frac{dN_b}{dt} = \frac{\eta_i I}{qV_{barr}} - R_b\,(N_b) - \frac{N_b}{\tau_{capt}} + \frac{N_w V_{act}}{V_{barr}}\frac{N}{\tau_{em}} \tag{22}$$

$$\frac{dN}{dt} = \frac{V_{barr}}{N_w V_{act}}\frac{N_b}{\tau_{capt}} - \frac{N}{\tau_{em}} - R_w(N) - \Gamma_c v_{gr}\frac{\alpha(N)}{\phi(S)}S \tag{23}$$

$$\frac{dS}{dt} = -\frac{S}{\tau_p} + N_w R_{w\beta}(N) + N_w \Gamma_c v_{gr}\frac{\alpha(N)}{\phi(S)}S \tag{24}$$

$$\frac{S}{P_f} = \frac{\lambda \tau_p}{\eta_c V_{act} hc} = \vartheta \tag{25}$$

Carrier-dependent gain $\alpha(N) = G_0 ln\left(\frac{R_w(N)}{R_w(N_0)}\right)$

Gain Saturation $\phi(S) = \frac{1}{1+\varepsilon\Gamma_c S}$

The ABC model which is used in [33] for evaluating carrier recombination rate in QW and SCH is unable to consider a complete portion of injection efficiency as this term is dependent upon incomplete capture of carriers into the active region and carrier escape from the active region [36]. Hence, the ABC model is inadequate to describe the steep drop in peak optical power and efficiency of III-nitride based lasers. In order to depict this droop phenomenon extensively, the ABC + *f(N)* model is introduced to scrutinize the mechanism of carrier recombination inside QW and SCH [37]. *A*, *B* and *C* are the unimolecular, radiative and Auger recombination coefficient; *f(N)* denotes carrier escape from active region.

$$\text{QW recombination rate } R_W(N) = AN + BN^2 + CN^3 + C_{DL,W}N^3 + D_{DL,W}N^4 \tag{26}$$

$$\text{SCH recombination rate } R_b(N_b) = A_b N_b + B_b {N_b}^2 + C_b {N_b}^3 + C_{DL,b}{N_b}^3 + D_{DL,b}{N_b}^4 \tag{27}$$

In "(26)" and "(27)", C_{DL} and D_{DL} are coefficients related with reduction in injection efficiency due to electrons drift leakage. δ is assumed as 0.1%.

$$C_{DL} = \frac{\delta\mu_n}{\mu_p p_{po}} B \tag{28}$$

$$D_{DL} = \left(\frac{\delta\mu_n}{\mu_p p_{po}}\right)^2 B \tag{29}$$

In "(28)" and "(29)", majority carrier concentration p_{po} is connected with temperature T and energy bandgap E_g as follows:

$$p_{po} = (N_c N_v)^{1/2} exp\left(\frac{-E_g}{2kT}\right) \tag{30}$$

$$N_c = 2\left(\frac{2\pi m_e^* kT}{h^2}\right)^{3/2};\ N_v = 2\left(\frac{2\pi m_h^* kT}{h^2}\right)^{3/2}$$

The electron and hole mobility for GaN and InN as a function of doping concentration N and temperature T is given by "(31)".

$$\mu_0(T,N) = \mu_{min}(T/300)^{\beta_1} + \frac{(\mu_{max} - \mu_{\min})\left(\frac{T}{300}\right)^{\beta_2}}{1 + \left[\frac{N}{N_{ref}\left(\frac{T}{300}\right)^{\beta_3}}\right]^{\sigma\left(\frac{T}{300}\right)^{\beta_4}}} \tag{31}$$

Reference density N_{ref} is taken as 10^{17} cm^{-3}. Required parameter values for "(31)" are adopted from [38]. The electron and hole mobility for $In_{0.17}Ga_{0.83}N$ QW and GaN SCH are then linearly interpolated from GaN and InN mobility values using Vagard's law to be used in "(28)" and "(29)".

$R_{W\beta}(N) = \beta_A AN + \beta_B BN^2 + \beta_C CN^3$; β_A, β_B and β_C are coupling constants.

Photon lifetime τ_p is given by: $\tau_p^{-1} = v_{gr}\left[\alpha_i + \frac{\ln\left(\frac{1}{R_m}\right)}{L_c}\right]$.

Here, α_i = internal cavity loss, L_c = cavity length and R_m = average reflectivity.

Output power coupling constant is calculated by:

$$\eta_c = 0.5ln\left(\frac{1}{R_m}\right)/[\alpha_i L_c + ln\left(\frac{1}{R_m}\right) \tag{32}$$

Equation (22) links the rate of change of carrier density N_b in the SCH layer with the pumping current I, rate of recombination in SCH and the interchange of carrier within the QW and SCH layers—i.e., the rate of carrier capture and emission by QW. Equation (23) connects the rate of change in carrier concentration N to the SCH layer carrier capture rate, carrier emission from QW, rate of recombination in QW and the stimulated-emission rate. Equations (24) and (25) define density of photon S and lasing power P_f. From "(22)" to "(25)", lasing wavelength λ, carrier-dependent gain $\alpha(N)$, gain coefficient G_o, optical transparency density N_o, group velocity v_{gr} and photon lifetime τ_p are crystal orientation dependent.

The following 3rd-order state-space model is applied with a view to simulating frequency response [30]. Appendix B shows the components of this state-space model.

$$\begin{bmatrix} \dot{N}_b \\ \dot{N} \\ \dot{S} \end{bmatrix} = \begin{bmatrix} \frac{\partial\left(\frac{dN_b}{dt}\right)}{\partial N_b} & \frac{\partial\left(\frac{dN_b}{dt}\right)}{\partial N} & \frac{\partial\left(\frac{dN_b}{dt}\right)}{\partial S} \\ \frac{\partial\left(\frac{dN}{dt}\right)}{\partial N_b} & \frac{\partial\left(\frac{dN}{dt}\right)}{\partial N} & \frac{\partial\left(\frac{dN}{dt}\right)}{\partial S} \\ \frac{\partial\left(\frac{dS}{dt}\right)}{\partial N_b} & \frac{\partial\left(\frac{dS}{dt}\right)}{\partial N} & \frac{\partial\left(\frac{dS}{dt}\right)}{\partial S} \end{bmatrix} \begin{bmatrix} N_b \\ N \\ S \end{bmatrix} + \begin{bmatrix} \frac{\eta_i}{qV_{barr}} \\ N \\ S \end{bmatrix} I$$

$$y = [0\,0\,1]\begin{bmatrix} N_b \\ N \\ S \end{bmatrix} \tag{33}$$

Relevant material parameters [39–43] in order to assess P-I response are listed in Table 2.

Table 2. Relevant parameters used for evaluating P-I characteristics.

Symbol (Unit)	Quantity	Value
η_i	Current-injection efficiency	0.86
Γ_c	Optical confinement factor	0.029
V_{act} (m^3)	Volume of one QW	4×10^{-19}
η_c	Output power coupling coefficient	0.51
ε	Phenomenological gain-saturation term	5×10^{-17}
A_W (s^{-1})	QW unimolecular recombination constant	3.3×10^7
A_b (s^{-1})	SCH unimolecular recombination constant	1×10^7
C_W (cm^{-6} s^{-1})	Auger recombination constant in QW	3.5×10^{-31}
C_b (cm^{-6} s^{-1})	SCH Auger recombination constant	1.4×10^{-31}
B_W (cm^3 s^{-1})	QW Radiative recombination constant	3.06×10^{-10}
B_b (cm^3 s^{-1})	SCH radiative recombination constant	1.1×10^{-8}
β_B	Radiative recombination coupling	1×10^{-4}
V_{barr} (m^3)	Volume of SCH	3×10^{-17}
τ_{cap} (ps)	QW capture lifetime	4
τ_{em} (ps)	emission lifetime of QW	6
α_i (cm^{-1})	Internal loss of the cavity	42
L_c (µm)	Cavity length	200
R_m	Mean mirror reflectivity	0.995

3. Results and Discussion

Following the numerical method described in Section 2, the optoelectronic performance of WZ $In_{0.17}Ga_{0.83}N$/GaN SQW blue laser was investigated in polar (0001), non-polar $(10\overline{1}0)$ and semipolar $(10\overline{1}2)$, $(11\overline{2}2)$ and $(10\overline{1}1)$ crystal orientations as a function of strain and related PZ field and QCSE. In the case of the proposed laser structure, the well was compressively strained for the selected In composition. Figure 5 depicts the strain tensor components as a function of crystal angle θ (inclination angle) of the growth axis to c-axis. From Figure 5, a noteworthy variation in the strain tensor elements is visualized for $0° < \theta < 90°$. Here, the strain component ε_{yy} is constant (−0.019) and independent of angle θ as realized from "(9)". The strain component ε_{xz} is zero for the (0001) and $(10\overline{1}0)$ orientation ($\theta = 0°$ and 90°) which means the in-plane strain is isotropic for polar crystal orientation. The strain components ε_{xx} and ε_{zz} show a maximum at $\theta = 0°$ and $\theta = 90°$, respectively.

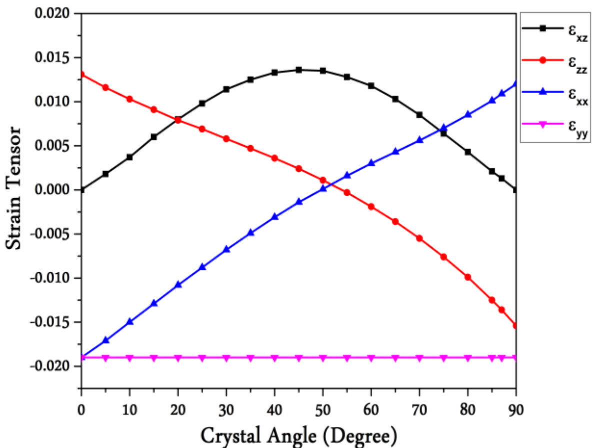

Figure 5. Strain tensor components as a function of crystal angle for 17% In composition.

The internal field for PZ polarization along the growth direction z′ can be computed from the strain tensors. The strain-assisted PZ polarization and SP polarization normal with respect to (w.r.t) QW plane is plotted in Figure 6a as a function of the crystal angle between the $In_{0.17}Ga_{0.83}N$/GaN SQW growth axis and the c-axis. The normal polarization is crucial due to quantized energy levels of QW structures along the growth direction. Because of this normal polarization, charge carriers accumulate at the heterointerface and generate an internal electric field. As seen from Figure 6a, the normal polarization is asymmetric w.r.t in the (10$\bar{1}$0) orientation (θ = 90°). Topmost normal polarization was observed for (0001) orientation (θ = 0°) due to larger compressive strain; then, it indicated a change in sign with an increasing crystal angle and became negative for $\theta = 58° < \theta < 90°$ range due to smaller strain. The internal field is shown in Figure 6b as a function of angle θ. It is seen that the internal field gradually increased and changed its sign with increasing crystal angle. Since the SP and strain-assisted PZ polarizations were zero for the (10$\bar{1}$0) crystal orientation, zero internal field was obtained in this orientation. In addition, the internal field was assessed to be zero near the crystal angle of 58°, as the sum of PZ and SP polarizations in the well was equal to that in the barrier. Thus, lasing characteristics for these crystal orientations (for example, (11$\bar{2}$2) semipolar orientation corresponding to 58.4° for $In_{0.17}Ga_{0.83}$ N/GaN QW) were anticipated to be largely improved due to the vanishing PZ polarization field and related QCSE.

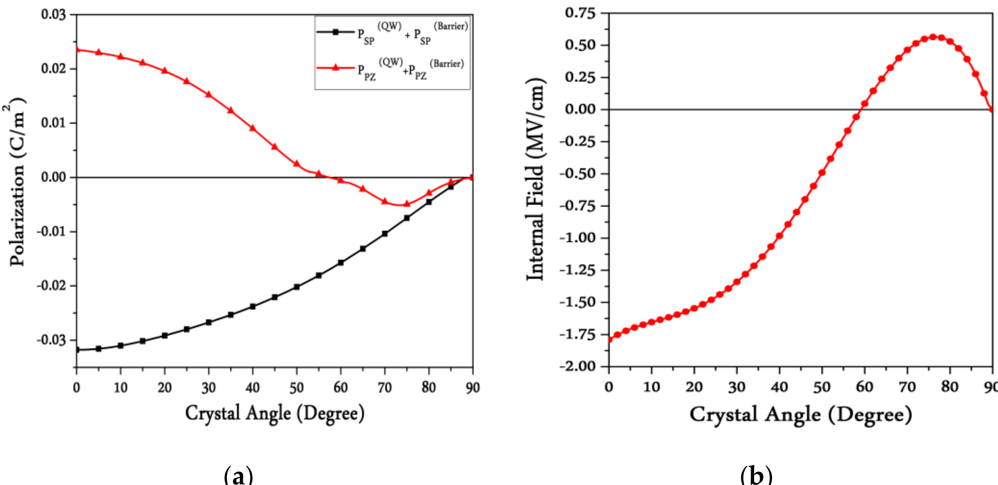

Figure 6. (**a**) The strain-assisted normal piezoelectric and spontaneous polarization w.r.t growth plane for $In_{0.17}Ga_{0.83}N$ QW and GaN barrier and (**b**) the internal electric filed as a function of crystal angle θ between the growth direction of QW and the c-axis.

Using the values of strain tensor components and internal polarization field, the energy band dispersion profile for (a) (0001) (θ = 0°), (b) (10$\bar{1}$0) (θ = 90°), (10$\bar{1}$2) (θ = 43°), (11$\bar{2}$2) (θ = 58.4°) and (10$\bar{1}$1) (θ = 62°) crystal orientations of WZ $In_{0.17}Ga_{0.83}N$/GaN QW blue laser were reckoned by solving 6 × 6 k·p RSP Hamiltonian at Γ-point and plotted in Figure 7. The figures are plotted with the same scale of the vertical and horizontal axis with a view to compare the orientation-dependent energies as a function of wave vector k. Here, conduction band, heavy hole, light hole and crystal field split off hole band dispersions are abbreviated as CB, HH, LH and CH, respectively. The conduction band in non-c-plane orientation was found to be parabolic as in a c-plane QW due to the nearly isotropic effective mass and spherically symmetric angular momentum Eigen-function of electrons. As seen from Figure 7, the increasing coupling from distant bands suggest strong anisotropy at the top valence band structure for non-polar and semipolar orientations unlike the polar (0001) c-plane for which a symmetric in-plane k_x-k_y band dispersion was observed. The result for non-polar (10$\bar{1}$0)-oriented QW structure shows small subband energy spacing between HH and LH. This strong band interaction eventually hindered fast movement of charge carriers prompting a reduction in lasing efficiency. On the other hand, semipolar (11$\bar{2}$2) and (10$\bar{1}$1) orientations showed an exquisite dispersion profile in

terms of decreased interband coupling and QCSE. This increase in subband energy spacing ultimately reduced the hole effective mass around the topmost valence band remarkably leading to improved emission characteristics.

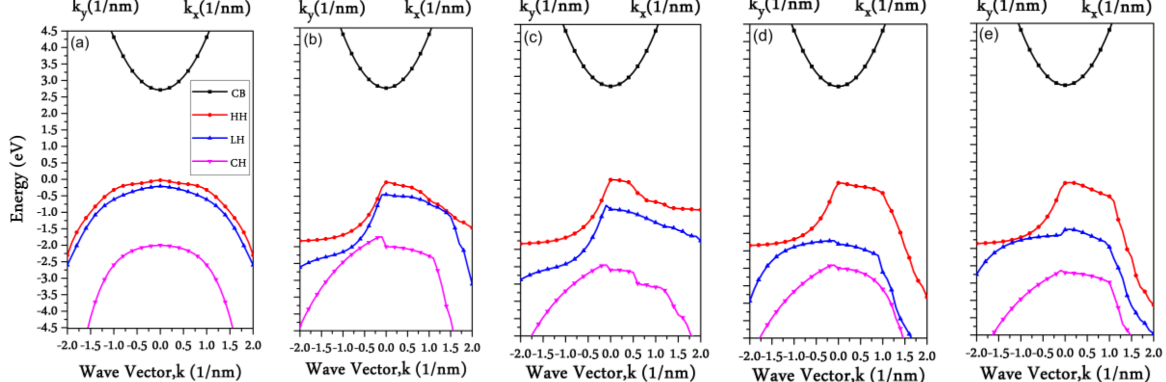

Figure 7. Energy band dispersion profile in (**a**) (0001), (**b**) $(10\bar{1}0)$, (**c**) $(10\bar{1}2)$ (**d**) $(11\bar{2}2)$ and (**e**) $(10\bar{1}1)$ crystal orientation of $In_{0.17}Ga_{0.83}N$/GaN QW blue laser.

The crystal orientation-dependent energy spacing between conduction band (CB)-heavy hole (HH), CB-light hole (LH) and HH-LH bands at the Γ-point were estimated in order to justify the optical emission profile and listed in Table 3. Because of allowed transition from CB to HH band, lasing emission occurred. Amid the intra-subbands, carrier tended to make a transition from CB to LH, whose probability decreased while the energy splitting between HH and LH was higher. The change in energy splitting was found to have strong dependence on crystal orientations. The Γ-point splitting between HH and LH was evaluated to be the maximum in semipolar $(11\bar{2}2)$ orientation and minimum in (0001) orientation, so better performance can be expected in semipolar $(11\bar{2}2)$ crystal orientation.

Table 3. Energy separation in different crystal orientation.

Crystal Orientation	CB-HH (eV)	CB-LH (eV)	HH-LH (eV)
(0001)	2.741	2.921	0.18
$(10\bar{1}2)$	2.702	3.552	0.85
$(11\bar{2}2)$	2.765	4.517	1.752
$(10\bar{1}1)$	2.824	4.174	1.35
$(10\bar{1}0)$	2.80	3.162	0.362

The TE and TM-polarized optical momentum matrix elements for the transition between CB-HH, CB-LH and CB-CH was derived from Γ-point Eigen values and plotted as a function of angle θ in Figure 8a,b. The interband momentum matrix elements from CB to HH and LH bands were controlled by TE polarization as shown in Figure 8a, and the interband transition from CB to CH band was mainly influenced by TM polarization, as seen in Figure 8b.The TE optical matrix element for CB-LH transition was seen to decrease rapidly with an increasing angle θ giving a minimum at 58°, and then showed a slight increase till 90°—i.e., $(10\bar{1}0)$ orientation. On the contrary, the TE optical matrix element for the CB-HH transition briskly escalated towards a maximum of 58° and then started to decrease till 90°. The peak value of momentum matrix was nearly 1.5 greater than that of the (0001) orientation. This is incontestably justified from the crystal orientation-dependent energy band dispersion profile of Figure 7. The minimal energy splitting between HH and LH bands and associated strong interband coupling for (0001) and $(10\bar{1}0)$ orientations effectively ceased quick carrier transition from VB to CB. On other side, since the HH-LH energy splitting was maximum at $(11\bar{2}2)$ orientation (θ = 58.4°), the optical momentum matrix for this orientation was near the highest value.

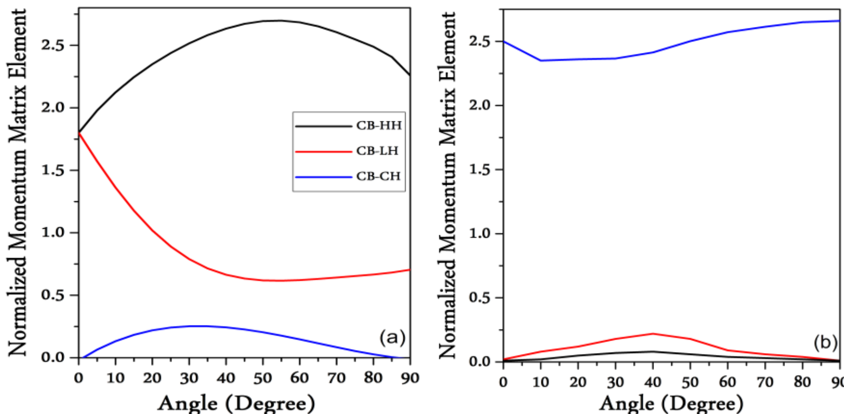

Figure 8. $In_{0.17}Ga_{0.83}$ N/GaN QW blue laser's optical momentum matrix elements normalized at Γ-point as a function of inclination angle θ for carrier transition from CB to HH, LH and CH due to (**a**) transverse electric (TE) and (**b**) transverse magnetic (TM) polarization.

The momentum matrix elements for CB-HH and CB-LH transitions in different crystal orientations as a function of wave vector k for TE polarization are illustrated in Figure 9a,b. For CB-HH transition, momentum matrix element in $(11\bar{2}2)$ orientation was maximum and lowest in (0001) orientation due to the overlaying function of holes and electrons, and the subsequent band mixing effect was highest and lowest in $(11\bar{2}2)$ and (0001) orientations, respectively. This phenomenon is justified from Figure 9b of CB-LH transition where maximum and minimum values of carrier transition probability were found in (0001) and $(11\bar{2}2)$ orientations.

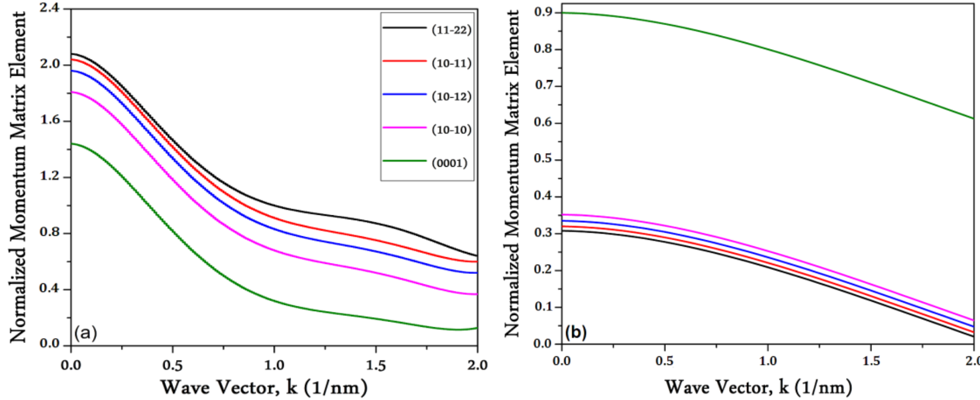

Figure 9. Momentum matrix elements normalized for (**a**) CB-HH transition and (**b**) CB-LH transition as a function of wave vector, k in different crystal orientations.

Figure 10 illustrates crystal orientation-dependent optical gain profile for TE polarization which was computed using "(19)". Topmost optical gains were assessed to be 1898, 2372, 2847, 4367 and 3701 cm^{-1} at wavelength λ of 452, 443, 459, 448 and 439 nm in (0001), $(10\bar{1}0)$, $(10\bar{1}2)$, $(11\bar{2}2)$ and $(10\bar{1}1)$ orientations, respectively. For $(11\bar{2}2)$ crystal orientation (θ = 58.4°), topmost gain was noticed because of the diminishing internal PZ polarization field and highest separation between HH and LH energy band, resulting in reduced QCSE and greater probability of transition from CB to HH. On the other hand, lowest gain was found in (0001) crystal orientation due to highest PZ polarization field and valence subband interaction and decreased probability of transition from CB to HH.

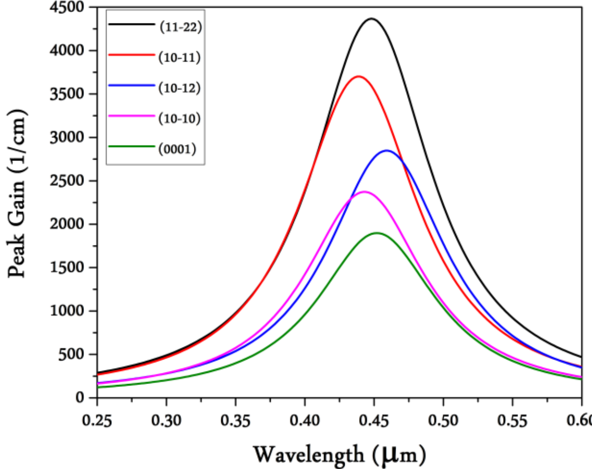

Figure 10. Orientation-dependent optical emission profile of $In_{0.17}Ga_{0.83}N/GaN$ QW blue laser.

Figure 11 demonstrates that TE-polarized optical gain in different crystal orientations relies upon the injection carrier density. The gain profile for ($11\overline{2}2$) and ($10\overline{1}1$)-oriented QW were very close to each other due to a small difference between their optical momentum matrix elements. Highest optical gain was observed in ($11\overline{2}2$) orientation and lowest in (0001) orientation. Additionally, threshold optical gain in a particular crystal orientation was found to be substantially dependent on the injection carrier density. The carrier density required to start gain was found to be smaller in ($11\overline{2}2$) orientation and higher in (0001) orientation.

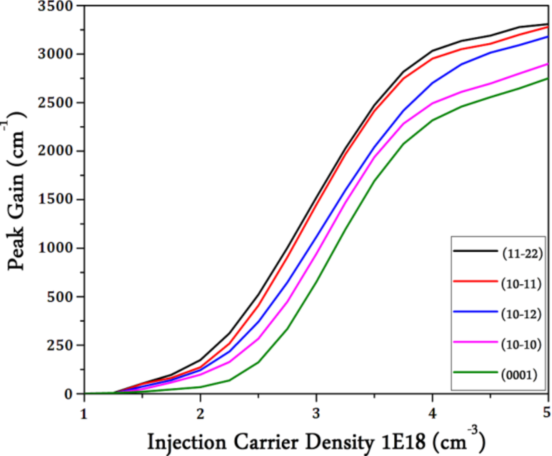

Figure 11. Optical gain in different crystal orientations depends on injection carrier density.

The differential gain at lasing wavelength is defined as the derivative of optical gain w.r.t charge carrier density in an active region calculated near the threshold point of stimulated emission. It is a crucial parameter in realizing efficient lasing operation since the relaxation oscillation frequency is assumed to be proportional to the square root of differential gain. The crystal orientation-dependent highest differential gain was calculated and shown in Table 4. Maximum differential gain of 6.34×10^{-16} cm^2 was found in ($11\overline{2}2$) crystal orientation at injection carrier density of 2.08×10^{18} cm^{-3}, and minimum differential gain of 4.35×10^{-16} cm^2 was found in (0001) crystal orientation at injection carrier density of 3.64×10^{18} cm^{-3}. So, higher carrier density is required to produce significant stimulated emission in polar c-plane crystal orientation than in semipolar and non-polar cases.

Table 4. Highest differential gain as a function of injection carrier density in TE mode.

Crystal Orientation	Differential Gain ($10^{-16}cm^2$)	Injection Carrier Density ($10^{18}cm^{-3}$)
(0001)	4.35	3.64
$(10\bar{1}2)$	5.32	3.02
$(11\bar{2}2)$	6.34	2.08
$(10\bar{1}1)$	6.26	2.13
$(10\bar{1}0)$	5.03	3.31

The impact of piezoelectric (PZ) field and related QCSE on $In_{0.17}Ga_{0.83}N$/GaN QW blue laser in terms of the CB minima, VB maxima and optical gain profile is encapsulated in Table 5. It's seen that for $(11\bar{2}2)$ and $(10\bar{1}0)$ orientation, the effect of PZ field is null which is verified from Figure 6. The shift in energy, peak gain and peak wavelength is evaluated maximum in (0001) orientation and minimum in $(10\bar{1}1)$ orientation.

Table 5. Effect of PZ field in different crystal orientation.

Crystal Orientation	PZ Field (MV/cm)	Peak Gain (cm^{-1})		Emission Wavelength (nm)		Conduction Band Energy Shifts, ΔE^c (meV)	HH Band Energy Shifts, ΔE^{hh} (meV)
		Without PZ Field	With PZ Field	Without PZ Field	With PZ Field		
(0001)	−1.79	4245	1898	443	452	0.5120	0.7315
$(10\bar{1}2)$	−0.85	4660	2847	452	459	0.1337	0.2927
$(11\bar{2}2)$	0	4880	4367	446	448	0	0
$(10\bar{1}1)$	+0.15	4800	3701	439	439	0.0824	0.1541
$(10\bar{1}0)$	0	4178	2372	438	443	0	0

Figure 12 presents optical power-injection current profile for compressively strained $In_{0.17}Ga_{0.83}N$/GaN SQW blue laser in polar, non-polar and semipolar crystal orientations. For different QW structures at lower input currents, the discrepancy between the optical powers is noticed to be comparatively smaller than those of at higher input currents. It is observed that slope efficiency for polar (0001) and semipolar $(10\bar{1}2)$ orientations are considerably less than semipolar $(10\bar{1}1)$ and $(11\bar{2}2)$ crystal orientations. This behavior can be attributed to their PZ field and associated band-bending and QCSE. As seen in Figure 6, there was a significant disparity in polarization charges between $In_{0.17}Ga_{0.83}N$ QW and GaN barriers. Again, only the carriers contained in QW were suited to contribute to radiative recombination plus stimulated emission produced by laser. The presence of large polarization field at the QW/barrier interface for polar c-plane and semipolar $(10\bar{1}2)$ orientations created a triangular barrier (Figure 1) which reduced carrier injection into the active region; it also aided the probability of carrier escape from the active region. The auger recombination rate also increased in comparison with radiative recombination, as it updated with square of density. This cumulative effect decreased carrier concentration in the QW, so reduced stimulated emission, optical gain and steep dropped in peak lasing power in these orientations. For non-polar $(10\bar{1}0)$ crystal orientation, the strong interband mixing effect is apparently the main reason behind low slope efficiency of P-I curve. As seen in Table 3, Γ-point splitting between HH and LH for this orientation was only 0.362 eV. This minimal energy splitting effectively ceased quick carrier transition from VB to CB, so decreased optical momentum matrix elements plus gain and drop in output power in this orientation. On the contrary, the effect of band bending and QCSE was negligible in semipolar $(11\bar{2}2)$ and $(10\bar{1}1)$ crystal orientations compared to others. It is noticed from Figure 12 that lowest threshold current of 1.45 mA and highest optical power of 4.08 mW were found in $11\bar{2}2$-oriented QW laser structure because of the highest gain plus optical momentum matrix elements for transition between CB to HH and lowest interband coupling between HH and LH in this orientation. Maximum threshold current of 2.75 mA was evaluated in (0001) crystal orientation. However, after close inspection, it was assumed that efficiency droop phenomenon is not a major concern for blue laser system operating at room temperature (300 K). In order to justify this

statement, a plot of external quantum efficiency (EQE) vs. injection current is displayed in Figure 13 for $(11\bar{2}2)$-oriented blue laser system at different temperature following the concept of [37]. As seen in this figure, efficiency droop was largest at 80 K. When the temperature was increased to 300 K, the efficiency droop was drastically reduced. This behavior can be explained by acknowledging "(28)" to "(31)". The terms C_{DL} and D_{DL} are strongly temperature-dependent. The majority of carrier concentration p_{po} degraded exponentially with drop in temperature. Charge carrier mobility μ_n and μ_p also reduced randomly with decreasing temperature. Since the term p_{po} overtook temperature-dependence of μ_n and μ_p, the value of C_{DL} and D_{DL} rose with the drop in temperature influencing steep droop in EQE. Additionally, with the fall in temperature, fermi energy gap increased (BGN) causing much less acceptors to ionize. This in turn, created discrepancy in carrier concentration, so EQE droop occurred at low injection currents for 80 K. However, the case was the opposite for 300 K. Reduction in fermi gap improved carrier transport between CB and VB, so higher carrier concentration and negligible EQE droop effect were observed.

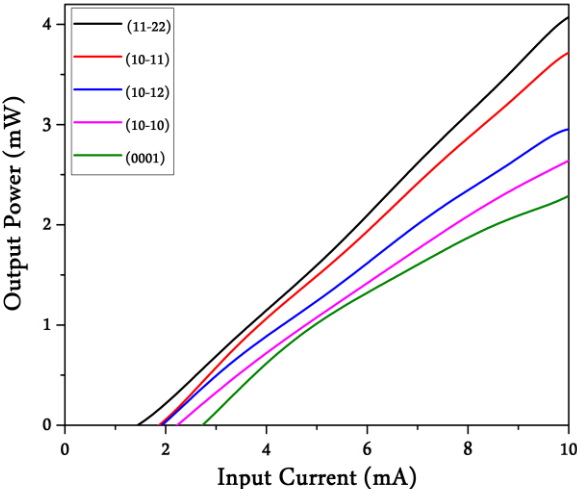

Figure 12. Orientation-dependent output power vs. input current characteristics.

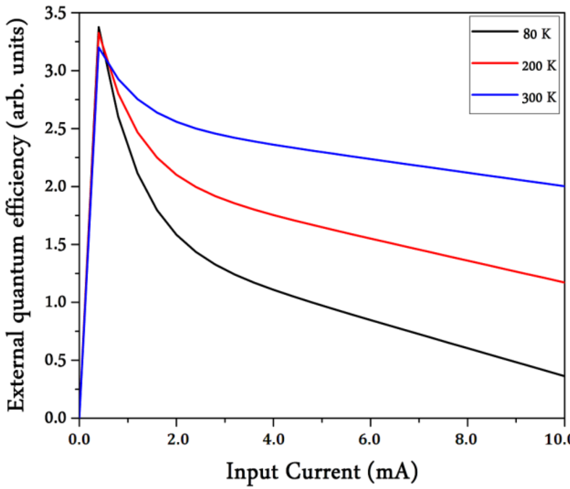

Figure 13. External quantum efficiency (EQE) vs. injection current at different temperatures for semipolar $(11\bar{2}2)$-oriented InGaN blue laser.

The P-I curve was analyzed near threshold in order to obtain operating points of Table 6 and use them to simulate frequency response following the state-space model of "(33)".

Table 6. Crystal orientation-dependent operating points close to threshold.

Crystal Orientation	Pumping Current (mA)	QW Electron Density N_{op} (cm^{-3})	SCH Electron Density N_{bop} (cm^{-3})	Photon Density S_{op} (cm^{-3})
(0001)	2.80	1.52×10^{16}	1.23×10^{15}	1.55×10^{9}
$(10\bar{1}0)$	2.30	1.57×10^{16}	1.26×10^{15}	1.29×10^{10}
$(10\bar{1}2)$	2.00	1.66×10^{16}	1.30×10^{15}	1.18×10^{11}
$(11\bar{2}2)$	1.50	1.80×10^{16}	1.39×10^{15}	1.07×10^{13}
$(10\bar{1}1)$	1.95	1.73×10^{16}	1.35×10^{15}	1.02×10^{12}

S_{op}, N_{op} and N_{bop} represent photon and electron densities (QW/SCH) for bias current close to the threshold point.

Figure 14 illustrates the Bode diagram in order to show magnitude (dB) and phase response of the $In_{0.17}Ga_{0.83}N$/GaN SQW blue laser in different crystal orientations. Since the Bode plot shows positive gain and phase margin in each orientation, the $In_{0.17}Ga_{0.83}N$/GaN SQW laser system for all orientations is stable. Highest and lowest magnitude (dB) response was obtained in semipolar $(11\bar{2}2)$ and polar (0001) crystal orientations because highest and lowest peak gain as well as optical output power were found in these orientations. From the aforementioned results, it is apparent that small rise time or fast response can be expected in semipolar $(11\bar{2}2)$ orientation (crystal growth angle of 58.4° w.r.t polar c-plane (0001) orientation) for the $In_{0.17}Ga_{0.83}N$/GaN QW blue laser.

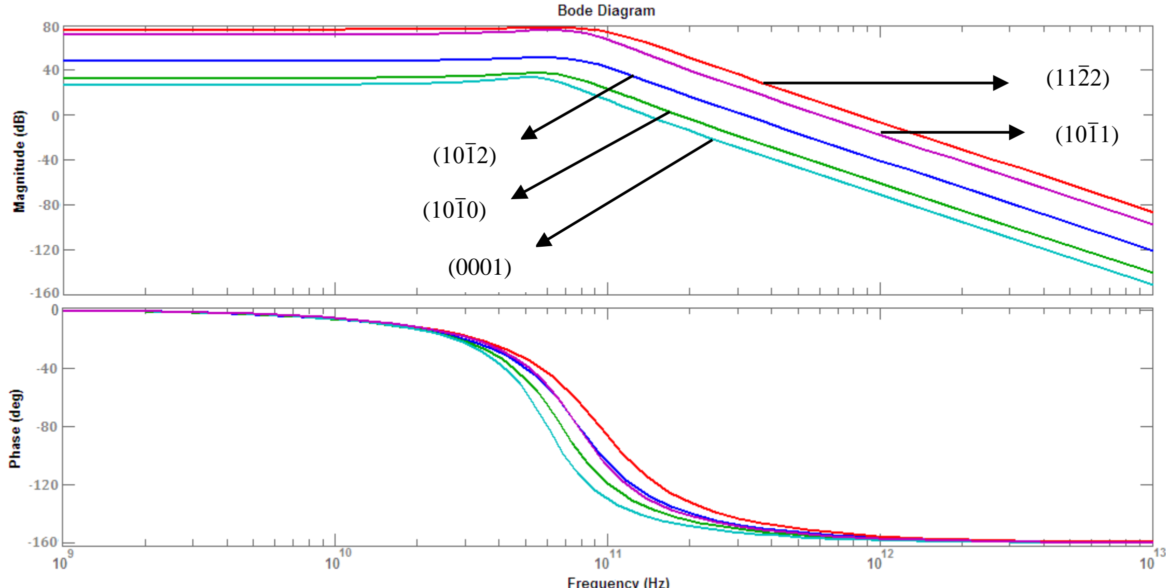

Figure 14. Frequency response of $In_{0.17}Ga_{0.83}N$/GaN SQW blue laser in different crystal orientation.

To confirm the validity of the proposed numerical approach, the results obtained from the simulation model are required to compare with the published results. Some elementary results on the InGaN QW blue laser in non-conventional orientation without including the impact of PZ field and related QCSE have been recorded [44]. To the best of the author's knowledge, there are no experimental or numerical results on optical gain profile and subsequent power-current and frequency response characteristics for the InGaN/GaN QW true blue laser in non-polar and semipolar orientation, although there exists some experimental and theoretical results on optical gain and output power profile for the InGaN/GaN QW-based green laser (λ > 500 nm) in polar (0001) and semipolar $(20\bar{2}1)$ orientation [45–47]. Firstly, the P-I response for the $In_{0.26}Ga_{0.74}N$/GaN multi-QW (2 pairs) green laser in c-plane (0001) orientation (λ = 508 nm) was considered for verification [45] and shown in Figure 15. The threshold current density (J_{Th}) of 1.56 kA/cm^2 and peak output power of 56.4 mW were found for this laser system from our simulation; threshold current density of 1.85 kA/cm^2 and peak output power of 58 mW are reported in [45].

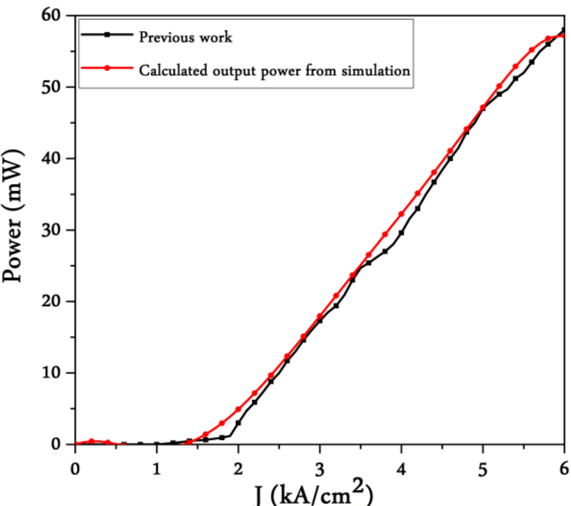

Figure 15. Comparison of output power vs. current curve for InGaN/GaN QW-based green laser (λ = 508 nm) calculated by our simulation model in polar (0001) orientation with the results reported in [45].

Secondly, the P-I response for the $In_{0.29}Ga_{0.71}N$/GaN double QW (DQW) green laser (λ = 525.5 nm) on semipolar $20\bar{2}1$-oriented GaN substrate was considered for verification [46] and shown in Figure 16. The threshold current of 43.7 mA and peak output power of 1.58 mW were found for this laser system from our simulation; threshold current of 51.1 mA and peak output power of 1.50 mW are reported [46]. So, both results in Figures 15 and 16 are in good agreement; the small discrepancy may be due to assumptions of some parameters which are not mentioned in [45] and [46].

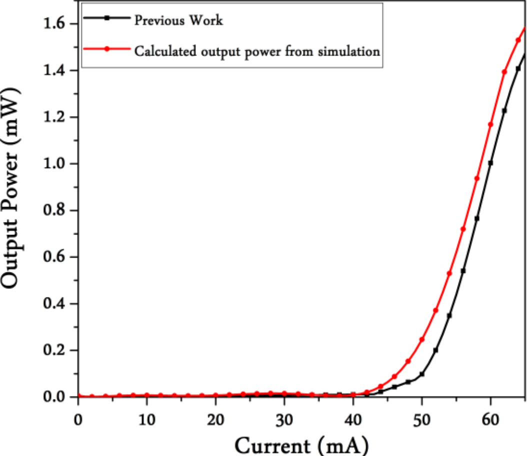

Figure 16. Comparison of output power vs. current curve for InGaN/GaN QW-based green laser (λ = 525.5 nm) calculated by our simulation model on semipolar $(20\bar{2}1)$-oriented GaN substrate with the results reported in [39]. The QW is along $(\bar{1}014)$ orientation.

Finally, the TE-polarized optical gain spectra for a 3 nm wide semipolar $20\bar{2}1$-oriented $In_{0.35}Ga_{0.65}N$ single QW on (0001)-oriented GaN substrate for charge carrier density of 7×10^{12} cm^{-2} was considered for verification [47] and shown in Figure 17. The topmost optical gain of 4990 cm^{-1} at lasing wavelength of 516 nm was found for this QW system from our calculation by "(17)", whereas topmost optical gain of 5150 cm^{-1} at lasing wavelength of 517 nm is reported in [47]. So, peak gain and emission wavelength at green region have good agreement. However, the photoluminance lineshape broadening was found to be higher in [47] than the lineshape obtained in Figure 17. This may be due to the inclusion of many

body effects in order to calculate optical gain spectra in [47] combining Coulomb-hole self-energy and Hartree–Fock energy correction.

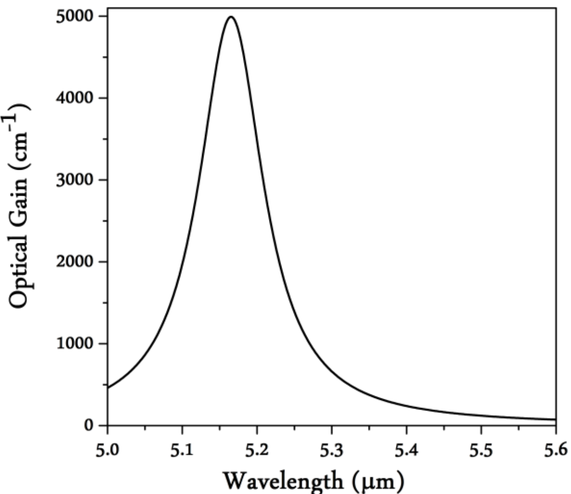

Figure 17. Calculated optical gain spectra for semipolar $(20\overline{2}1)$-oriented $In_{0.35}Ga_{0.65}N$ single QW for charge carrier density of 7×10^{12} cm^{-2}.

4. Conclusions

To recapitulate, the key optoelectronic performance of $In_{0.17}Ga_{0.83}N$/GaN QW blue laser was studied numerically in conventional polar c-plane (0001) orientation as well as in non-polar $(10\overline{1}0)$ and semipolar $(10\overline{1}2)$, $(11\overline{2}2)$ and $(10\overline{1}1)$ orientations with the application of six-band k.p Hamiltonian and successive Euler's rotation technique. The numerical results demonstrate that energy band dispersion profile, momentum matrix elements, optical gain, output lasing power and frequency response for different QW structures are strongly dependent on piezoelectric field and crystal orientations. Energy splitting between conduction and valence subbands was seen to be higher in semipolar $(11\overline{2}2)$ crystal orientation. Highest lasing power output and lowest threshold current were attained for $(11\overline{2}2)$ crystal orientation because piezoelectric polarization-induced quantum confined stark effect in this orientation was zero. The inspection of frequency response revealed that highest magnitude (dB) response was also achieved for the semipolar $(11\overline{2}2)$-oriented QW laser structure. In conjunction with these, the verification of our current numerical approach with some of the published results on InGaN QW-based green laser in non-c-plane orientation confirms that the semipolar $(11\overline{2}2)$-oriented $In_{0.17}Ga_{0.83}N$/GaN QW blue laser is expected to be a promising light source for high-speed free space optical communication systems.

Author Contributions: Conceptualization, M.R.I. and A.H.H.; Formal analysis, S.R. and S.G.K.; Methodology, S.R.; Software, S.R. and S.G.K.; Supervision, M.R.I.; Validation, L.F.A., M.M.R. and M.S.I.; Visualization, P.N.R., M.S.R., L.F.A., I.M.M. and M.S.I.; Writing—original draft, S.R. and M.M.R.; Writing—review and editing, P.N.R., M.M.H., M.S.R. and M.B.H.; All authors have read and agreed to the published version of the manuscript.

Funding: This research received no external funding.

Conflicts of Interest: The authors declare no conflict of interest.

Appendix A

The output power is obtained by using the simulation model of Figure A1 with I as input parameter from a signal generator and S, N, N_b, and P_f as output parameters. The ramp input signal is applied to the sum block-1 of Figure A1. It is added to the pumping current I to generate the electrical impulse of the laser diode. The components connected with the upper sum block-2 (bigger sum) simulate the carrier density rate equation in active and SCH layers. So, it is possible to capture the output of carrier density from the end of these two blocks. Photon Density comes from the output of the lower sum

block-3 connected with the lower bigger sum block-4. It is also converted to power output in watts by using "(23)". All simulations use a standard 4th-order Runge-Kutta algorithm with a fixed step size of 1ps as an equation solver.

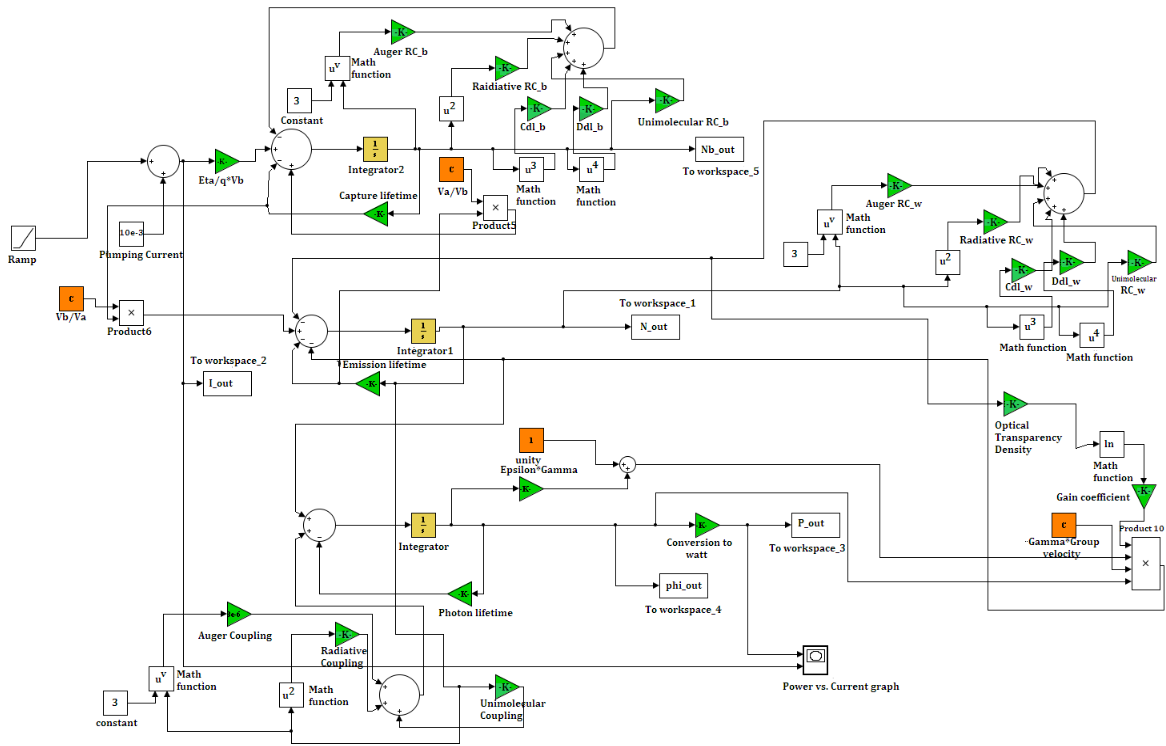

Figure A1. Simulation model to obtain output power vs. input current curve.

Appendix B

In order to find values to simulate the frequency response, an arbitrary point is chosen near the threshold value of the P-I response curve such that the gain saturation term $\phi(S)$ will approach 1 for values of $\varepsilon\Gamma_c S \ll 1$. Then, the non-linear rate equations from "(20)" to "(22)" are linearized for constructing the state-space model of "(25)" by taking the partial derivative of each time-dependent term with respect to photon and electron density. The components of "(25)" are shown below:

$$\frac{\partial(dN_b/dt)}{\partial N_b} = \frac{-1}{\tau_{capt}} - (A_b + 2B_b N_{bop} + 3C_b N_{bop}^2 + 3C_{DL,b} N_{bop}^2 + 4D_{DL,b} N_{bop}^3)$$

$$\frac{\partial(dN_b/dt)}{\partial N} = \frac{V_{act}}{V_{barr} * \tau_{em}}$$

$$\frac{\partial(dN_b/dt)}{\partial S} = 0$$

$$\frac{\partial(dN/dt)}{\partial N_b} = \frac{V_{barr}}{V_{act} * \tau_{capt}}$$

$$\frac{\partial(dN/dt)}{\partial N} = \frac{-1}{\tau_{em}} - \left(A + 2BN_{op} + 3CN_{op}^2 + 3C_{DL,w} N_{op}^2 + 4D_{DL,w} N_{op}^3\right) - \Gamma_c v_{gr} Q S_{op}$$

$$\frac{\partial(dN/dt)}{\partial S} = -\Gamma_c v_{gr} G_0 \ln\left(\frac{AN_{op} + BN_{op}^2 + CN_{op}^3 + C_{DL,w} N_{op}^3 + D_{DL,w} N_{op}^4}{R_w(N_0)}\right)$$

$$\frac{\partial(dS/dt)}{\partial N_b} = 0$$

$$\frac{\partial(dS/dt)}{\partial N} = \left(\beta_A A + 2\beta_B B N_{op} + 3\beta_C C N_{op}^2\right) + \Gamma_c v_{gr} Q S_{op}$$

$$\frac{\partial(dS/dt)}{\partial S} = \frac{-1}{\tau_p} + \Gamma_c v_{gr} G_0 \ln\left(\frac{AN_{op} + BN_{op}^2 + CN_{op}^3 + C_{DL,w}N_{op}^3 + D_{DL,w}N_{op}^4}{R_w(N_0)}\right)$$

$$Q = \frac{G_0 S}{AN_{op} + BN_{op}^2 + CN_{op}^3 + C_{DL,w}N_{op}^3 + D_{DL,w}N_{op}^4}\left(A + 2BN_{op} + 3CN_{op}^2 + 3C_{DL,w}N_{op}^2 + 4D_{DL,w}N_{op}^3\right)$$

References

1. Zhou, C.; Ghods, A.; Saravade, V.G.; Patel, P.V.; Yunghans, K.L.; Ferguson, C.; Feng, Y.; Kucukgok, B.; Lu, N.; Ferguson, I.T. Review:The Current and Emerging Applications of the {III}-Nitrides. *ECS J. Solid State Sci. Technol.* **2017**, *6*, Q149–Q156. [CrossRef]
2. Morkoç, H.; Strite, S.; Gao, G.B.; Lin, M.E.; Sverdlov, B.; Burns, M. Large-band-gap SiC, III-V nitride, and II-VI ZnSe-based semiconductor device technologies. *J. Appl. Phys.* **1994**, *76*, 1363–1398. [CrossRef]
3. Osawa, H.; Yamamoto, H.; Miura, Y.; Sasao, W.; Ino, Y.; Satoh, H.; Satoh, K.; Sugano, K. Blue Laser Imaging Provides Excellent Endoscopic Images of Upper Gastrointestinal Lesions. *Video J. Encycl. GI Endosc.* **2014**, *1*, 607–610. [CrossRef]
4. Moustakas, T.D.; Paiella, R. Optoelectronic device physics and technology of nitride semiconductors from the {UV} to the terahertz. *Rep. Prog. Phys.* **2017**, *80*, 106501. [CrossRef]
5. Shuji Nakamura, S.P. Fasol The Blue Laser Diode. The Complete Story. *Meas. Sci. Technol.* **2001**, *12*, 755–756. [CrossRef]
6. Feneberg, M.; Thonke, K. Polarization fields of {III}-nitrides grown in different crystal orientations. *J. Phys. Condens. Matter* **2007**, *19*, 403201. [CrossRef]
7. Wetzel, C.; Amano, H.; Akasaki, I. Piezoelectric Polarization in {GaInN}/{GaN} Heterostructures and Some Consequences for Device Design. *Jpn. J. Appl. Phys.* **2000**, *39*, 2425–2427. [CrossRef]
8. Feezell, D.; Sharma, Y.; Krishna, S. Optical properties of nonpolar III-nitrides for intersubband photodetectors. *J. Appl. Phys.* **2013**, *113*, 133103. [CrossRef]
9. Rass, J.; Wernicke, T.; Scheibenzuber, W.G.; Schwarz, U.T.; Kupec, J.; Witzigmann, B.; Vogt, P.; Einfeldt, S.; Weyers, M.; Kneissl, M. Polarization of eigenmodes in laser diode waveguides on semipolar and nonpolar GaN. *Phys. Status Solidi Rapid Res. Lett.* **2010**, *4*, 1–3. [CrossRef]
10. Li, H.; Zhang, H.; Li, P.; Wong, M.S.; Chow, Y.C.; Pinna, S.; Klamkin, J.; DeMierry, P.; Speck, J.S.; Nakamura, S.; et al. Development of efficient semipolar {InGaN} long wavelength light-emitting diodes and blue laser diodes grown on a high quality semipolar {GaN}/sapphire template. *J. Phys. Photonics* **2020**, *2*, 31003. [CrossRef]
11. Zhang, H.; Li, H.; Li, P.; Song, J.; Speck, J.S.; Nakamura, S.; DenBaars, S.P. Room-Temperature Continuous-Wave Electrically Driven Semipolar ($20\bar{2}\bar{1}$) Blue Laser Diodes Heteroepitaxially Grown on a Sapphire Substrate. *ACS Photonics* **2020**, *7*, 1662–1666. [CrossRef]
12. Cao, Y.; Dzuba, B.; Magill, B.A.; Senichev, A.; Nguyen, T.; Diaz, R.E.; Manfra, M.J.; McGill, S.; Garcia, C.; Khodaparast, G.A.; et al. Photoluminescence study of non-polar m-plane InGaN and nearly strain-balanced InGaN/AlGaN superlattices. *J. Appl. Phys.* **2020**, *127*, 185702. [CrossRef]
13. Xing, K.; Tseng, C.; Wang, L.; Chi, P.; Wang, J.; Chen, P.; Liang, H. Semi-polar ($11\bar{2}2$) GaN epitaxial films with significantly reduced defect densities grown on m-plane sapphire using a sequence of two in situ SiNx interlayers. *Appl. Phys. Lett.* **2019**, *114*, 131105. [CrossRef]
14. Senichev, A.; Dzuba, B.; Nguyen, T.; Cao, Y.; Capano, M.A.; Manfra, M.J.; Malis, O. Impact of growth conditions and strain on indium incorporation in non-polar m-plane ($10\bar{1}0$) InGaN grown by plasma-assisted molecular beam epitaxy. *APL Mater.* **2019**, *7*, 121109. [CrossRef]
15. Sawicka, M.; Feduniewicz-Żmuda, A.; Kryśko, M.; Turski, H.; Muziol, G.; Siekacz, M.; Wolny, P.; Skierbiszewski, C. Indium incorporation in semipolar ($20\bar{2}1$) and nonpolar ($10\bar{1}0$) InGaN grown by plasma assisted molecular beam epitaxy. *J. Cryst. Growth* **2017**, *459*, 129–134. [CrossRef]
16. Song, J.; Choi, J.; Xiong, K.; Xie, Y.; Cha, J.J.; Han, J. Semipolar (2021) GaN and InGaN light-emitting diodes grown on sapphire. *ACS Appl. Mater. Interfaces* **2017**, *9*, 14088–14092. [CrossRef]

17. Tronciu, V.Z.; Yamada, M.; Abram, R.A. Analysis of the dynamics of a blue-violet InGaN laser with a saturable absorber. *Phys. Rev. E* **2004**, *70*, 26604. [CrossRef]
18. Okuno, Y.; Aoki, M.; Tsuchiya, T.; Uomi, K. Fabrication of (001) InP-based 1.55-µm wavelength lasers on a (110) GaAs substrate by direct bonding (A prospect for free-orientation integration). *Appl. Phys. Lett.* **1995**, *67*, 810–812. [CrossRef]
19. Okuno, Y. Investigation on direct bonding of III–V semiconductor wafers with lattice mismatch and orientation mismatch. *Appl. Phys. Lett.* **1996**, *68*, 2855–2857. [CrossRef]
20. Okuno, Y.; Uomi, K.; Aoki, M.; Tsuchiya, T. Direct wafer bonding of III-V compound semiconductors for free-material and free-orientation integration. *IEEE J. Quantum Electron.* **1997**, *33*, 959–969. [CrossRef]
21. Moses, P.G.; de Walle, C.G. Band bowing and band alignment in InGaN alloys. *Appl. Phys. Lett.* **2010**, *96*, 21908. [CrossRef]
22. Sarkar, N.; Ghosh, S. Temperature dependent band gap shrinkage in GaN: Role of electron–phonon interaction. *Solid State Commun.* **2009**, *149*, 1288–1291. [CrossRef]
23. Wu, J.; Walukiewicz, W.; Shan, W.; Yu, K.M.; Ager Iii, J.W.; Li, S.X.; Haller, E.E.; Lu, H.; Schaff, W.J. Temperature dependence of the fundamental band gap of InN. *J. Appl. Phys.* **2003**, *94*, 4457–4460. [CrossRef]
24. Chuang, S.L. *Physics of Photonic Devices*; John Wiley & Sons: Hoboken, NJ, USA, 2012; Volume 80.
25. Chuang, S.L.; Chang, C.S. k.p method for strained wurtzite semiconductors. *Phys. Rev. B* **1996**, *54*, 2491–2504. [CrossRef]
26. Park, S.-H.; Chuang, S.-L. Crystal-orientation effects on the piezoelectric field and electronic properties of strained wurtzite semiconductors. *Phys. Rev. B* **1999**, *59*, 4725–4737. [CrossRef]
27. Bykhovski, A.; Gelmont, B.; Shur, M.; Khan, A. Current-voltage characteristics of strained piezoelectric structures. *J. Appl. Phys.* **1995**, *77*, 1616–1620. [CrossRef]
28. Chuang, S.L.; Chang, C.S. Effective-mass Hamiltonian for strained wurtzite GaN and analytical solutions. *Appl. Phys. Lett.* **1996**, *68*, 1657–1659. [CrossRef]
29. Smith, D.L.; Mailhiot, C. Piezoelectric effects in strained-layer superlattices. *J. Appl. Phys.* **1988**, *63*, 2717–2719. [CrossRef]
30. Bastard, G.; Mendez, E.E.; Chang, L.L.; Esaki, L. Variational calculations on a quantum well in an electric field. *Phys. Rev. B* **1983**, *28*, 3241–3245. [CrossRef]
31. Ohtoshi, T.; Kuroda, T.; Niwa, A.; Tsuji, S. Dependence of optical gain on crystal orientation in surface-emitting lasers with strained quantum wells. *Appl. Phys. Lett.* **1994**, *65*, 1886–1887. [CrossRef]
32. Hasan, M.M.; Islam, M.R.; Teramoto, K. Crystallographic orientation-dependent optical properties of GaInSb mid-infrared quantum well laser. *Optik (Stuttg)* **2012**, *123*, 1993–1997. [CrossRef]
33. Vurgaftman, I.; Meyer, J.R.; Ram-Mohan, L.R. Band parameters for III–V compound semiconductors and their alloys. *J. Appl. Phys.* **2001**, *89*, 5815–5875. [CrossRef]
34. Schaer, T.; Rusnov, R.; Eagle, S.; Jastrebski, J.; Albanese, S.; Fernando, X. A dynamic simulation model for semiconductor laser diodes. In Proceedings of the CCECE 2003—Canadian Conference on Electrical and Computer Engineering. Toward a Caring and Humane Technology (Cat. No.03CH37436), Montreal, QC, Canada, 4–7 May 2003; Volume 1, pp. 293–297.
35. Mena, P.V.; Kang, S.-M.; DeTemple, T.A. Rate-equation-based laser models with a single solution regime. *J. Light. Technol.* **1997**, *15*, 717–730. [CrossRef]
36. Feng, M.X.; Sun, Q.; Liu, J.P.; Li, Z.C.; Zhou, Y.; Gao, H.W.; Zhang, S.M.; Yang, H. A study of efficiency droop phenomenon in GaN-based laser diodes before lasing. *Materials* **2017**, *10*, 482. [CrossRef]
37. Cho, J.; Schubert, E.F.; Kim, J.K. Efficiency droop in light-emitting diodes: Challenges and countermeasures. *Laser Photon. Rev.* **2013**, *7*, 408–421. [CrossRef]
38. Nawaz, M.; Ahmad, A. A {TCAD}-based modeling of {GaN}/{InGaN}/Si solar cells. *Semicond. Sci. Technol.* **2012**, *27*, 35019. [CrossRef]
39. Piprek, J.; Sink, R.K.; Hansen, M.A.; Bowers, J.E.; DenBaars, S.P. Simulation and optimization of 420-nm InGaN/GaN laser diodes. In Proceedings of the Physics and Simulation of Optoelectronic Devices VIII; Binder, R.H., Blood, P., Osinski, M., Eds.; SPIE: San Jose, CA, USA, 2000; Volume 3944, pp. 28–39.
40. Piprek, J. *Nitride Semiconductor Devices: Principles and Simulation*; Wiley Online Library: Berlin, Gremany, 2007; Volume 590.

41. Fan, W.H.; Olaizola, S.M.; Wang, T.; Parbrook, P.J.; Wells, J.-P.R.; Mowbray, D.J.; Skolnick, M.S.; Fox, A.M. Carrier capture times in InGaN/GaN multiple quantum wells. *Phys. Status Solidi* **2003**, *240*, 364–367. [CrossRef]
42. Lang, J.R.; Young, N.G.; Farrell, R.M.; Wu, Y.-R.; Speck, J.S. Carrier escape mechanism dependence on barrier thickness and temperature in InGaN quantum well solar cells. *Appl. Phys. Lett.* **2012**, *101*, 181105. [CrossRef]
43. Yu, H.; Lee, L.K.; Jung, T.; Ku, P.C. Photoluminescence study of semipolar $\{10\bar{1}1\}$ InGaN/GaN multiple quantum wells grown by selective area epitaxy. *Appl. Phys. Lett.* **2007**, *90*, 141906. [CrossRef]
44. Roy, S.; Islam, M.R.; Hasan, M.M.; Hossain, S.A. Crystallographic orientation-dependent performance of 445 nm InGaN Blue Laser. In Proceedings of the 2016 9th International Conference on Electrical and Computer Engineering (ICECE), Dhaka, Bangladesh, 20–22 December 2016; pp. 307–310.
45. Tian, A.; Liu, J.; Zhang, L.; Li, Z.; Ikeda, M.; Zhang, S.; Li, D.; Wen, P.; Zhang, F.; Cheng, Y.; et al. Green laser diodes with low threshold current density via interface engineering of InGaN/GaN quantum well active region. *Opt. Express* **2017**, *25*, 415–421. [CrossRef]
46. Adachi, M.; Yoshizumi, Y.; Enya, Y.; Kyono, T.; Sumitomo, T.; Tokuyama, S.; Takagi, S.; Sumiyoshi, K.; Saga, N.; Ikegami, T.; et al. Low Threshold Current Density InGaN Based 520–530 nm Green Laser Diodes on Semi-Polar {2021} Free-Standing GaN Substrates. *Appl. Phys. Express* **2010**, *3*, 121001. [CrossRef]
47. Scheibenzuber, W.G. *GaN-Based Laser Diodes: Towards Longer Wavelengths and Short Pulses*; Springer Science & Business Media: Freiburg, Germany, 2012.

Publisher's Note: MDPI stays neutral with regard to jurisdictional claims in published maps and institutional affiliations.

© 2020 by the authors. Licensee MDPI, Basel, Switzerland. This article is an open access article distributed under the terms and conditions of the Creative Commons Attribution (CC BY) license (http://creativecommons.org/licenses/by/4.0/).